Engineering Failure Analysis 148 (2023) 107133

Contents lists available at ScienceDirect

Engineering Failure Analysis

journal homepage: www.elsevier.com/locate/engfailanal

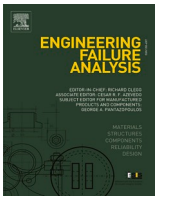

8-MW wind turbine tower computational shell buckling benchmark. Part 2: Detailed reference solution

Adam J. Sadowski [a,*], Marc Seidel [b]

[a] Department of Civil and Environmental Engineering, Imperial College London, United Kingdom
[b] Siemens Gamesa Renewable Energy GmbH & Co. KG, Germany

ARTICLE INFO

Keywords:
Wind turbine support tower
Buckling
Plastic collapse
GMNIA
EN 1993-1-6
Verification
Calibration
Finite element analysis

ABSTRACT

An assessment of the elastic–plastic buckling limit state for multi-strake wind turbine support towers poses a particular challenge for the modern finite element analyst, who must competently navigate numerous modelling choices related to the tug-of-war between meshing and computational cost, the use of solvers that are robust to highly nonlinear behaviour, the potential for multiple near-simultaneously critical failure locations, the complex issue of imperfection sensitivity and finally the interpretation of the data into a safe and economic design.

This paper presents a detailed reference solution to the computational buckling analysis of a standardised benchmark problem of an 8-MW multi-strake wind turbine support tower. Both linear and nonlinear analyses are performed, including advanced GMNIA with several different models of geometric imperfections. The crucial issue of interpreting the imperfection amplitude in a way that is compliant with the new prEN 1993-1-6 is discussed in detail. The solution presented herein is intended for use by analysts in both industry and academia for training, verification and calibration of finite element models and is intended to initiate a public repository of such computational solutions for metal civil engineering shell structures.

This paper is the second of a pair. The first paper [37] presents a synthesis of 29 submissions to an international round-robin exercise performed on the same benchmark problem.

1. Introduction

In 2016, a pan-European group of experts were tasked by CEN/TC250/SC3 to work on formalising the use of finite element analysis in structural steel design. Although when the first meeting took place in 2017 this was still an Ad-Hoc Group working on what was then intended to be either a 'Technical Document' or an Annex to an existing Eurocode, by 2019 it had morphed into a formal Working Group 22 of SC3 working on the first drafts of an entirely new prEN 1993-1-14 on the design of steel structures assisted by finite element analysis. In 2021, an advanced document was circulated for CEN Enquiry. This entirely new Eurocode is an important document aiming to standardise the often very inconsistent choices made by finite element analysts, namely those relating to geometry, meshing, material laws and solver settings, in recognition of the increasingly important role that computational predictions are playing in modern structural design. It has also provided a valuable impetus for the accumulation of computational benchmark problems for the verification or calibration of finite element models and methodologies, for which it has established a formal protocol.

It should be recognised that the EN 1993-1-6 Eurocode on the strength and stability of metal shells has had standardised rules for

* Corresponding author.
E-mail address: a.sadowski@imperial.ac.uk (A.J. Sadowski).

https://doi.org/10.1016/j.engfailanal.2023.107133
Received 29 December 2022; Received in revised form 6 February 2023; Accepted 13 February 2023
Available online 17 February 2023

design of shell structures assisted by finite element analysis since at least the ENV in 1995, and that its drafting committee (which included Prof. Herbert Schmidt (University of Duisburg-Essen), Prof. Michael Rotter (University of Edinburgh) and Prof. Richard Greiner (TU Graz)) was the progenitor of the extremely successful LA, LBA, MNA, GMNA, GMNIA taxonomy since adopted into prEN 1993-1-14 and by the wider structural steel community. The interested reader will find detailed historical information in the ECCS EDR5#2 [1] book of recommendations that accompanied the 2007 version of EN 1993-1-6 [2]. Present in drafts of ENV 1993-1-6 [3] since as early as 1995 have also been detailed rules aiming to validate or verify finite element models against 'known results', in response to specific concerns raised by Prof. Richard Greiner in recognition of the ease with which catastrophic mistakes can be made during modelling and design. Specifically, for the design of metal civil engineering shell structures assisted by the most advanced nonlinear GMNIA, it has long been required by ENV/ EN 1993-1-6 that a 'reliability check' be performed to assess the ability of the analyst to reproduce a 'known' result on a similar system to the one being designed. The analyst's computed resistance for that 'known' system $R_{GMNIA,check}$ (scaling factor on the applied load set to achieve failure) is then either validated against a test result R_{test} (whose geometric imperfections must be representative of those that occur in practical construction and which the analyst should have made some effort to include in their model) or verified against a 'well-established known resistance from the literature' $R_{k,known}$ (implicitly taken to either mean an algebraic result or a carefully conducted and widely accepted finite element result). The available resistances are then combined to give a calibration factor k_{GMNIA} such that

$$k_{GMNIA} = \frac{R_{test}}{R_{GMNIA,check}} \text{ or } \frac{R_{k,known}}{R_{GMNIA,check}} \tag{1}$$

which is used to calibrate the computed GMNIA resistance R_{GMNIA} of the actual system being designed to give a characteristic resistance R_k and thence a design resistance R_d.

$$R_k = k_{GMNIA} \cdot R_{GMNIA} \text{ from which } R_d = \frac{R_k}{\gamma_{M1}} \tag{2}$$

where γ_{M1} is the partial factor for resistance of a shell to the buckling ultimate limit state. If the 'known value' is used, the calibration factor must be in the range $0.8 < k_{\mathrm{GMNIA}} < 1.2$ to be acceptable, while if a test result is used the restriction is $k_{\mathrm{GMNIA}} \leq 1$.

A recent meta study of the available test results of axially compressed cylinders from the publicly available scientific literature by Sadowski *et al.* [4]) revealed that this entire body of experimental data is unrepresentative of full-scale civil engineering construction and sparsely documented, and a similar situation likely exists for other reference shell systems. While that study made the case that these tests would be an entirely inappropriate dataset upon which to calibrate safety–critical partial factors such as γ_{M1}, it *could* have had some value as a source of provisional examples for individual finite element model validation through k_{GMNIA} factors. Unfortunately, for this to have been possible the tests would have needed to be accompanied by very detailed imperfection measurements. With the limited exception of the numerous buckling tests that formed the now-defunct Initial Imperfection Databank (IIDB) [5,6], in which well-documented destructive buckling tests were accompanied by surface imperfection surveys, such detailed information is essentially unobtainable. Indeed, a recent computational study by Kathirkamanathan *et al.* [7] showed that even the resolution of the surface scans of isotropic specimens in the IIDB is too low to have captured all of the key buckling-relevant imperfection features likely to have existed in the actually tested specimens (and other important types of imperfection may not have been measured at all), and that with this information alone it is not consistently possible to computationally obtain buckling resistances as low as those reported from these tests. Using such test results to calibrate k_{GMNIA} would lead to penalisingly low computed R_k through no fault of the analyst which would only serve to discourage the use of GMNIA in design. Consequently, calibration of k_{GMNIA} on R_{test} from tests is unlikely to be attractive for as long as test data of appropriate quantity and quality are not available, which only leaves $R_{k,known}$ from 'well-established known resistances from the literature' as a feasible option. It should be stated, finally, that the γ_{FE} 'model factor covering the uncertainties of the numerical model and the executed analysis type' introduced by prEN 1993-1-14 [8] is a direct descendant of the k_{GMNIA} factor from EN 1993-1-6 albeit recast into a probabilistic framework.

Given the emphasis now placed in prEN 1993-1-6 [9] and prEN 1993-1-14 [8] on the calibration of finite element models used for safety–critical civil engineering structural design, and the fact that over two decades have passed since the first drafts of EN 1993-1-6, it is rather surprising that the publicly available repository of well-documented benchmark solutions involving shell structures is still relatively sparse. What is available for shells is typically limited to algebraic stress analyses or linear bifurcation solutions of relatively simple reference axisymmetric systems such as individual cylinders (the interested reader may consult the 'blue book' of Teng and Rotter [10]), although a handful of nonlinear computational studies can be used for more complex benchmarking (see for example [1,11,12]). For realistic full-scale civil engineering metal structures, however, a public repository of solutions with sufficient detail to be fully reproducible is virtually non-existent.

The worked solution to the international 'round-robin' exercise benchmark presented here is intended to form the start of such a repository and permit analysts to directly calibrate a k_{GMNIA} for this particular class of shell structure. It was already present in the companion paper [37] where it was referred to as a 'reference solution' and highlighted with heavy black icons or curves on combined comparison plots. Its consistent placement inside or close to the interquartile range of all submission gives strong support for it being a correct solution within the bounds of the modelling assumptions that have been made. The Reader is cautioned, however, that the analyses detailed here are intended purely for individual model verification and do not necessarily represent an exhaustive set of analyses necessary to certify a structural design. Such a set must follow the full provisions of the necessary Eurocodes which are too numerous to be all mentioned here. The Authors encourage constant vigilance and double-checking during the modelling process.

Table 1
Geometry of the top segment of an 8 MW wind turbine support tower.

Strake ID	h (mm)	r_1 (top) (mm)	r_2 (bottom) (mm)	t (mm)	β (rads)	ρ_1 (top) (mm)	ρ_2 (bottom) (mm)
Flange 101	600	2072.50	2072.50	50	0	2072.50	2072.50
Strake 102	2319	2072.50	2128.95	13	0.02434	2073.11	2129.58
Strake 103	2569	2128.95	2196.70	13	0.02637	2129.69	2197.46
Strake 104	2684	2196.70	2267.55	14	0.02639	2197.47	2268.34
Strake 105	2675	2267.55	2338.10	14	0.02637	2268.34	2338.91
Strake 106	2416	2338.10	2401.85	14	0.02638	2338.91	2402.69
Strake 107	2657	2401.85	2471.95	14	0.02638	2402.69	2472.81
Strake 108	2648	2471.95	2541.85	15	0.02639	2472.81	2542.74
Strake 109	2639	2541.85	2611.45	15	0.02637	2542.73	2612.36
Strake 110	2630	2611.45	2680.85	15	0.02638	2612.36	2681.78
Strake 111	2621	2680.85	2750.00	15	0.02638	2681.78	2750.96
Strake 112	2068	2750.00	2750.00	15	0	2750.00	2750.00
Strake 113	2067	2750.00	2750.00	16	0	2750.00	2750.00
Strake 114	2368	2750.00	2750.00	16	0	2750.00	2750.00
Strake 115	2897	2750.00	2750.00	17	0	2750.00	2750.00
Flange 116	142	2750.00	2750.00	17	0	2750.00	2750.00

2. The benchmark

The benchmark problem documented in this paper is identical to that set as part of the international round-robin exercise explored in the companion paper [37], and only a repeat of the most pertinent information is given here. The benchmark is based on the upper 36 m long segment being close to a real design of an 8-MW multi-strake steel wind turbine support tower, though the modelled segment itself is assumed to be fully fixed at the base.

The individual heights h, cross-sectional upper r_1 and lower r_2 radii and thicknesses t are presented in Table 1, together with the angle of incline of the meridian to the vertical β and the upper ρ_1 and lower ρ_2 circumferential radii of curvature calculated as $\rho = r \cdot \sec\beta$. The nominal material is a S355J0 grade steel, throughout with an elastic modulus of 210 GPa, a Poisson ratio of 0.3, a nominal yield strength of 345 MPa and a density of 7850 kg/m^3. Two load cases (LCs) are considered, both including gravity-induced self-weight. The first (LC1) consists of a transverse force $Q = 1.76$ MN, a bending moment $M = 33$ MNm acting in the same direction and a vertical force $V = 4$ MN, all acting through a centroidal location within the top Flange 101. In the second (LC2), $Q = 1.6$ MN, $M = 30$ MNm, $V = 4$ MN and there is an additional global torsional moment $T = 22$ MNm. Readers may refer to Fig. 2 of the companion paper [37] for an illustration of the geometry and loads, as well as Fig. 1 here.

3. Modelling of the tower

3.1. Meshing protocol

The mesh design adopted here for every computational analysis follows the meshing protocol of Sadowski [13] which built on the work of Spagnoli [14] on axially compressed conical shells. The protocol assumes that the smallest theoretically possible buckles in both conical and cylindrical shells are those under axial (meridional) compression, and that this is the scale of the smallest meaningful buckling-relevant feature for which the mesh should be purposefully designed for conical and cylindrical shell structures under general loading. In particular, the theoretical device of the generalised Koiter ellipse may be used to establish upper bounds for critical linear bifurcation buckling modes with the maximum possible number of meridional half-waves m_{max} and circumferential full waves n_{max} respectively. The Koiter ellipse is defined as

$$\bar{m}^2\rho_{avg}^2 + n^2\sec^2\beta - \frac{\pi\sqrt{2}}{a}\bar{m}\rho_{avg}\sqrt{\frac{\rho_{avg}}{t}} = 0 \tag{3}$$

where $a = \frac{\pi}{\sqrt[4]{3(1-\nu^2)}} \approx 2.444$ for $\nu = 0.3$, $\bar{m} = m\frac{L}{\pi}$ & $\rho_{avg} = \frac{1}{2}(\rho_1 + \rho_2) = \frac{1}{2}(r_1 + r_2)\sec\beta$ from which it can be shown that

$$m_{\max} = \frac{\sqrt{2}}{a} \cdot \frac{L}{\sqrt{\rho_{avg} t}} \approx 0.579\frac{L}{\sqrt{\rho_{avg} t}} \tag{4}$$

and

$$n_{\max} = \frac{\pi}{a\sqrt{2}} \cdot \cos\beta\sqrt{\frac{\rho_{avg}}{t}} \approx 0.909\cos\beta\sqrt{\frac{\rho_{avg}}{t}} \tag{5}$$

for $\nu = 0.3$. Adopting a reasonable 'rule of thumb' that the buckling half-wavelength in either direction should be discretised by a minimum of 10 linear shell elements (although the analyst is free to vary this), the minimum mesh resolution along the meridian M_{min}

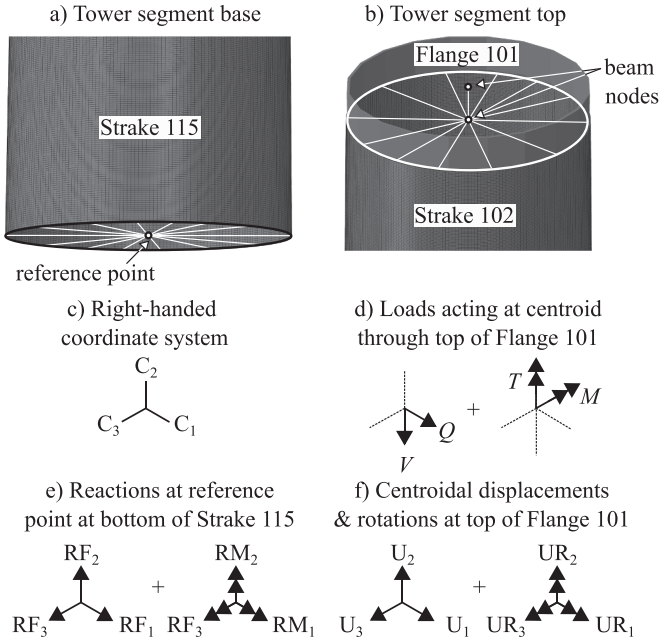

Fig. 1. Modelling details, coordinate system, *dofs* and reactions.

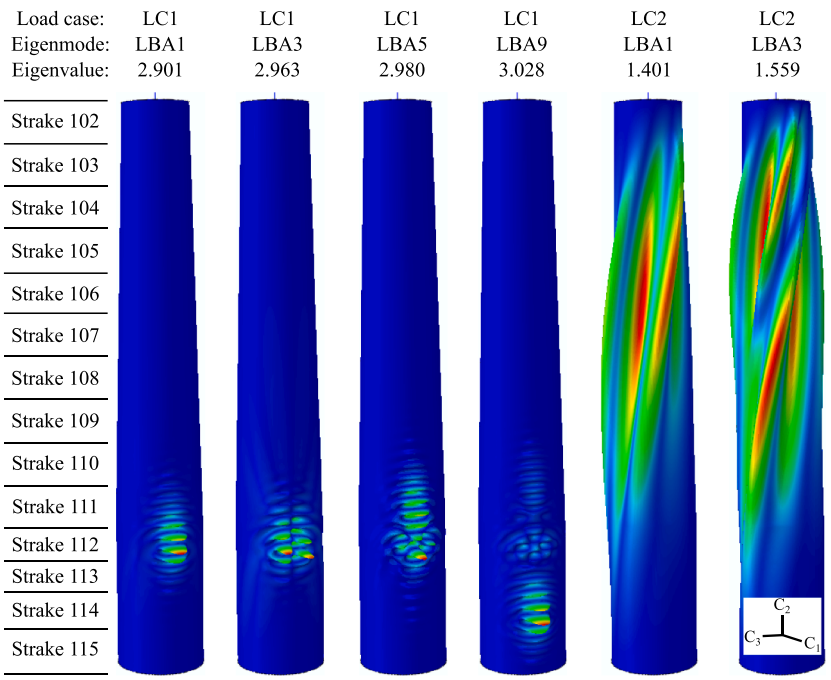

Fig. 2. Selection of LBA eigenmode shapes for both load cases.

Table 2
Mesh design for the tower segment.

Strake ID	ρ_{avg} (mm)	m_{max}	n_{max}	M_{min}	N_{min}
Flange 101	*n/a*	*n/a*	*n/a*	*n/a*	*n/a*
Strake 102	2101.35	8.12	11.55	82	232
Strake 103	2163.58	8.87	11.72	89	235
Strake 104	2232.90	8.79	11.48	88	230
Strake 105	2303.63	8.62	11.66	87	234
Strake 106	2370.80	7.68	11.82	77	237
Strake 107	2437.75	8.33	11.99	84	240
Strake 108	2507.77	7.90	11.75	80	235
Strake 109	2577.55	7.77	11.91	78	239
Strake 110	2647.07	7.64	12.07	77	242
Strake 111	2716.37	7.52	12.23	76	245
Strake 112	2750.00	5.89	12.31	59	247
Strake 113	2750.00	5.70	11.92	58	239
Strake 114	2750.00	6.53	11.92	66	239
Strake 115	2750.00	7.75	11.56	78	232
Flange 116	*n/a*	*n/a*	*n/a*	*n/a*	*n/a*
					Overall: $N = 247$

or circumference N_{min} of any individual conical shell strake may be taken as:

$$M_{\min} = \lceil 10 \cdot m_{\max} \rceil \approx \lceil 5.8 \frac{L}{\sqrt{\rho_{avg} t}} \rceil \tag{6}$$

and

$$N_{\min} = \lceil 10 \cdot 2n_{\max} \rceil \approx \lceil 18.2 \cos\beta \sqrt{\frac{\rho_{avg}}{t}} \rceil \tag{7}$$

for $\nu = 0.3$ where the partial brackets represent the *ceil* operation (round upwards to nearest integer). While the theory behind the Koiter ellipse is linear, the predicted buckling eigenmodes are known to be similar in scale to nonlinear bifurcation buckles and the above procedure offers a convenient, geometrically scalable and programmable mesh design capability. It is cautioned that the resulting meshes may be finer than an analyst is accustomed to, but the resolution can be controlled by varying the number of elements per half-wavelength in Eqs (6) and (7). While the number of shell elements edges along the meridian M varies per strake (Table 2), to maintain mesh quality it is recommended to keep the number of shell edges around the circumference N constant as the maximum of all individual strake calculations using Eq. (7). This meshing scheme applies only to shell strakes and not to stiff flanges which, if they are not the focus of the analysis and if they are stiff enough to fully restrain cross-sectional ovalisation, may be simply modelled as circular hollow beam sections or rigid entities.

3.2. Modelling choices

The ABAQUS 2017 [15] commercial finite element software was used in all analyses presented here, but the methodology and modelling features should be entirely agnostic to the software used. Flange 116 is assumed to be superfluous to the structural response of the tower segment above it and was not included in this solution. Instead, the nodes along the bottom edge of Strake 115 were tied to a centroidal reference point via a rigid body kinematic coupling (Fig. 1a). All *dofs* of this reference point were restrained, leading to an effective BC1r boundary condition at the base of the modelled tower segment. Using a reference point in this manner is very convenient as it greatly simplifies the application of boundary conditions and the calculation of base reactions (which are then just taken as force and moment reactions at this reference point, thus avoiding an onerous integration of individual contributions from all nodes along the bottom circumference). Similarly, Flange 101 at the top of the tower was modelled as a circular hollow section beam element with the beam node at the 101–102 boundary linked to those of the top circumferential edge nodes of Strake 102 with a rigid body kinematic coupling (Fig. 1b). The point loads specified in the benchmark can then be easily applied to the beam element node at the top of Flange 101, and tip deflections and rotations can be obtained with similar ease. Use of a beam element for Flange 101 precludes any cross-sectional distortion of the top flange, a reasonable assumption for such a thick component. Further information on such 'hybrid' beam-shell models for tower structures may be found in Sadowski [13]. Following the mesh design summarised in Table 2, the mesh consists of 266,513 reduced-integration S4R linear shell elements for Strakes 102–115 and a single B31 linear beam element for Flange 101, for a total of 1,600,578 model *dofs*. Every input file was approximately 25 MB in size. A simple isotropic elastic material law was assumed for LA and LBA, while all (G)MN(I)A assumed an ideal elastic but rigid plastic formulation with a yield plateau but zero post-yield strain hardening for simplicity. However, the analyst may find a selection of material formulations permissible for use in GMNIA which include strain hardening in prEN 1993-1-14 [8].

These modelling details are illustrated in Fig. 1, together with the convention for a right-handed Cartesian coordinate system (where C_1 – C_3 identify the original nodal coordinates), nodal *dofs* (displacements U_1 – U_3 and rotations UR_1 – UR_3 in the right-hand

screw rule) and reactions (forces RF_1 – RF_3 and moments RM_1 – RM_3) adopted in this paper. The 2 axis is the vertical axis through the tower centreline. A radial nodal displacement U_ρ in the 1–3 axes' plane is occasionally convenient and may be computed from the Cartesian quantities as:

$$U_\rho = \sqrt{(C_1 + U_1)^2 + (C_3 + U_3)^2} - \sqrt{U_1^2 + U_3^2} \tag{8}$$

The generic nature of this notation is intended to aid analysts in easily relating these quantities to whatever coordinate system and naming convention is used by their software. Lastly, in all analyses the self-weight load caused by gravity was included in the load set that was scaled by the respective algorithm. While it would be more physically realistic to apply self-weight to full intensity as a 'pre-load' in an initial analysis step (geometrically linear for LBA and MNA, nonlinear for GMN(I)A) so that the resulting stress state can be perpetuated through the next analysis step where all other tower loads would be subsequently applied and scaled to failure, it is code-compliant in that self-weight is then treated the same as any other design load.

4. LA: Base reactions and tip *dofs*

The six reactions at the base centroidal reference point (Fig. 1a) and the six *dofs* at the top centroidal beam node of Flange 101 (Fig. 1b) are summarised in Table 3 for both load cases. These should serve as the first validation checkpoint. The mass of the tower model is 67.4136 t (0.66133 MN with $g = 9.81$ m/s^2) as reported by ABAQUS.

5. LBA: Reference elastic critical buckling resistances (eigenvalues) and eigenmodes

A summary of the ten lowest ('most critical') LBA eigenmodes and their corresponding eigenvalues is presented in Table 4 with a selection illustrated in Fig. 2. The eigenvalues are load proportionality factors on the set of design loads characterising both load sets, and the lowest ones for either LC give the reference elastic critical buckling resistance R_{cr} for that LC. If self-weight is omitted from the analyses entirely it results in eigenvalues only ~ 0.1 % higher and very similar eigenmodes. The addition of a torsional moment (and a minor change in two other loads) results in a significant reduction in R_{cr} (~52 %) and a qualitative change in the critical eigenmode. While this may imply that torsion may have an important effect on the resistance of the tower, this conclusion cannot be drawn without first additionally considering the effect of plasticity as will be presented shortly. The Lanczos eigensolver was used with the stipulation that only non-negative eigenvalues are to be reported (to avoid physically erroneous situations such as 'negative gravity', see discussion in the companion paper).

Although they are easy to compute, the eigenmode shapes presented in Fig. 2 should give the analyst significant pause if they are aiming to use them as equivalent geometric imperfections in GMNIA. For the non-torsional LC1 in particular, the critical eigenmode represents an imperfection localised in Strake 112 only which may or may not be globally critical if introduced into GMNIA. Higher-order eigenmodes would be necessary to obtain imperfections localised elsewhere (e.g. eigenmode no. 9 for Strake 114) and many hundreds of eigenmodes may need to be extracted at significant computational cost before a 'desired' localisation of buckling deformations is obtained (see discussion in Sadowski [13]). In any case, the claim for eigenmodes being representative of any manufacturing imperfections likely to arise in full-scale civil engineering towers is tenuous, and in this context the Reader is invited to consult the discussion by Rotter [16] of the different approaches to the design of imperfect shells against buckling. This discussion notwithstanding, the results of the LBA are revisited in detail in Sections 8 and 10 where they are used as equivalent geometric imperfections in GMNIA.

6. MNA: Reference plastic resistances and tip *dofs*

The MNAs were performed using the 'Riks' arc-length solver of ABAQUS with disabled geometric nonlinearity. The analysis step scaled the full set of design loads corresponding to either LC for exactly 100 increments with initial and maximum load proportionality factor (*LPF*) increments set at 0.1 (10 % of the intensity of the loads in the LC) and the algorithm being free to modify the increment size. Although terminating an MNA after a fixed number of increments does not guarantee that a fully-developed plastic collapse mechanism has been attained corresponding to a horizontal plateau on the equilibrium relationship, particularly for stress states involving significant through-thickness bending, this was a reasonable limit for the purposes of this illustration. The equilibrium paths of selected tip *dofs* vs the applied *LPF* are presented in Fig. 3 and demonstrate that while a significant plateau has developed after 100

Table 3
Summary of base centroidal reactions and tip centroidal *dofs* (reported to three significant figures based on single precision, see Fig. 1 for convention).

Base reaction	LC1	LC2	Tip *dof*	LC1	LC2
RF_1 [N]	-1.76×10^6	-1.60×10^6	U_1 [mm]	2.67×10^2	2.42×10^2
RF_2 [N]	4.66×10^6	4.66×10^6	U_2 [mm]	-3.20×10^0	-3.20×10^0
RF_3 [N]	-9.11×10^{-5}†	-7.35×10^{-5}†	U_3 [mm]	5.13×10^{-9}†	5.97×10^{-9}†
RM_1 [Nmm]	-2.64×10^0	-2.19×10^0	UR_1 [rad]	1.98×10^{-13}†	6.50×10^{-13}†
RM_2 [Nmm]	-6.90×10^{-1}	-2.20×10^{10}	UR_2 [rad]	1.70×10^{-13}†	7.24×10^{-3}
RM_3 [Nmm]	9.61×10^{10}	8.74×10^{10}	UR_3 [rad]	-1.48×10^{-2}	-1.35×10^{-2}

† represent values which are effectively negligible but have not been evaluated to exactly zero due to roundoff errors in the matrix solution procedure.

Table 4
Summary of LBA eigenvalues and eigenmodes for both load cases (reported to 4 significant figures).

Eigenmode	LC1 Eigenvalue	Vertical position of $\|U_{\rho,max}\|$ [mm]	Strake of $\|U_{\rho,max}\|$ [mm]	LC2 Eigenvalue	Vertical position of $\|U_{\rho,max}\|$ [mm]	Strake of $\|U_{\rho,max}\|$ [mm]
LBA1	2.901 ($\equiv R_{cr}$)	8138.2	Strake 112	1.401 ($\equiv R_{cr}$)	23818.7	Strake 106
LBA2	2.907	8313.4	Strake 112	1.401	23097.0	Strake 106
LBA3	2.963	8208.3	Strake 112	1.559	21393.0	Strake 107
LBA4	2.967	7998.0	Strake 112	1.559	28021.5	Strake 104
LBA5	2.980	7822.7	Strake 112	1.673	30860.7	Strake 103
LBA6	2.984	7998.0	Strake 112	1.673	31495.7	Strake 103
LBA7	3.020	7962.9	Strake 112	1.768	31611.2	Strake 103
LBA8	3.021	8173.2	Strake 112	1.768	16376.5	Strake 109
LBA9	3.028	3722.2	Strake 114	1.854	16511.8	Strake 109
LBA10	3.033	3901.6	Strake 114	1.854	14684.8	Strake 109

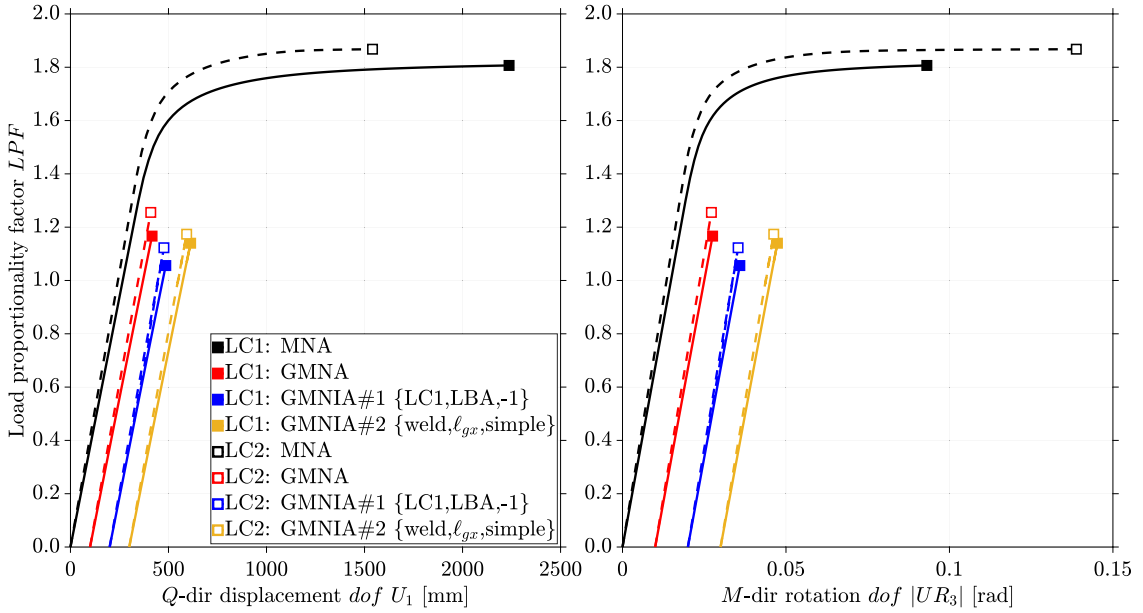

Fig. 3. Equilibrium plot of the *LPF* vs selected tip *dofs* for MNA, GMNA and two sets of representative GMNIAs for FTQC A (see Table 8: {LC1,LBA1,-1} for both LC1 and LC2, and weld depression relative to l_{gx} (simplified treatment)). Solid and white-fill squares represent critical load factors for LC1 and LC2 respectively, while solid and dashed lines represent equilibrium relationships for LC1 and LC2 respectively. Some curves have been separated out by a horizontal offset for enhanced readability.

increments, it is clearly not yet fully horizontal. A full discussion of this phenomenon including a procedure to estimate the reference plastic collapse load based on only a partially-computed equilibrium relationship may be found in Doerich and Rotter [17], with an automated implementation in Sadowski *et al.* [18], and more recently in dos Santos *et al.* [19].

The MNA reference plastic resistances R_{pl} were determined to be 1.807 and 1.868 for LC1 and LC2 respectively (taken as the last of the 100 increments, black circles in Fig. 3), which can be compared with the LBA reference elastic critical buckling resistances R_{cr} of 2.901 and 1.401 respectively. In both cases R_{pl} and R_{cr} are not too far apart suggesting that plasticity may play a significant role in the ultimate limit state, as will be demonstrated by subsequent GMN(I)A. The approximate plastic collapse mechanisms are illustrated on the left-hand side of Fig. 4, where collapse is primarily by the development of a plastic hinge at the junction of Strakes 111 and 112. The addition of torsion and modification of M and Q loads has a relatively minor effect, serving only to create an additional plastic hinge at the bottom of Strake 103, in significant contrast to the effect of torsion on R_{cr}.

7. GMNA: Buckling resistances and tip *dofs*

The GMNAs were performed under similar solver settings as the MNAs with the input files being identical except for the geometric nonlinearity flag being activated for both analysis steps and the initial and maximum *LPF* increments set to 0.05 (5 % of the intensity of the loads in the LC). The GMNA resistances were determined to be $R_{GMNA} = 1.167$ and 1.256 for LC1 and LC2 respectively on the basis of the bifurcation load factor on the computed equilibrium curve (C2 criterion in prEN 1993-1-6), representing a significant reduction

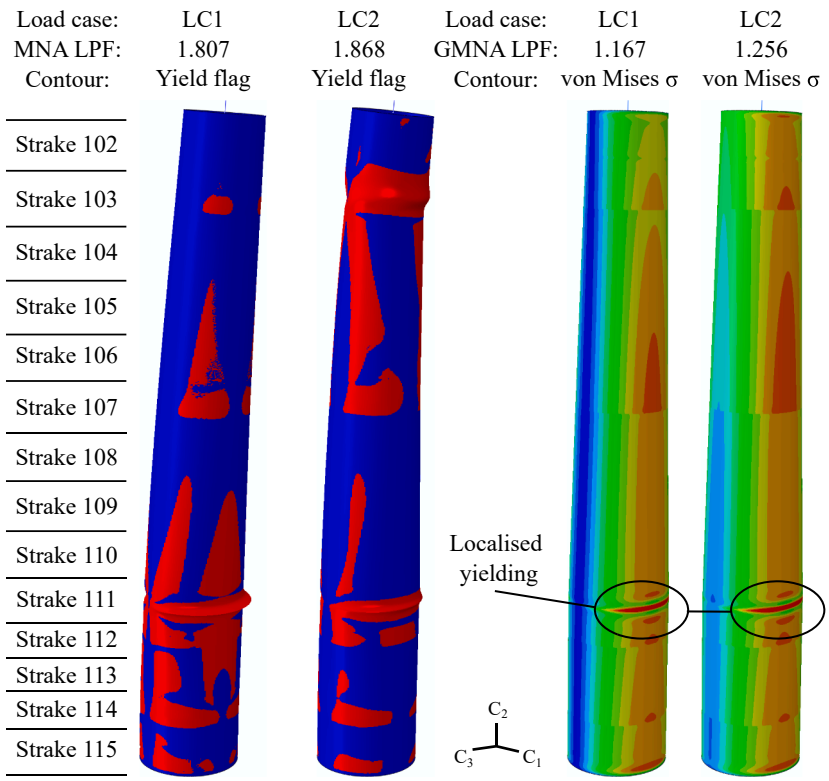

Fig. 4. MNA plastic collapse mechanisms (with yielded regions in red) and GMNA deformed shape at buckling (von Mises stress contours) for both load cases (inner shell surface conditions). (For interpretation of the references to colour in this figure legend, the reader is referred to the web version of this article.)

in resistance relative to MNA owing to the additional influence of geometric nonlinearity. Remarkably, the change from LC1 to LC2 only has a minor effect on the GMNA result as the von Mises stress state at buckling is very similar as illustrated by the contour plots on the right-hand side of Fig. 4.

It is likely that both towers fail initially by localised elastic–plastic buckling at the junction of Strakes 111 and 112, the same location where MNA predicted plastic collapse by the development of a plastic hinge. The equilibrium relationship (red curves in Fig. 3) suggests a very linear pre-buckling response and a sudden and likely catastrophic elastic–plastic bifurcation buckling event. However, under the present analysis conditions it was not possible to follow the equilibrium path beyond the onset of the first buckling event, and no post-buckling increments could be obtained (red lines in Fig. 3). This results in a slight blurring of the distinction between the C1 (max. load factor on curve) and *C*2 (bifurcation load factor) criteria in prEN 1993-1-6, but it is acceptable here because it is obvious from the circumstances that a bifurcation must have been reached. As discovered in the companion paper [37], the general inability of modern nonlinear quasi-static finite element solvers to reliably follow the equilibrium path beyond the first critical buckling event appears to be a regrettable feature of most commercial software packages, a consequence of the basic path-tracing solvers having received little further development in recent decades.

8. GMNIA #1 with LBA eigenmode imperfections: Amplitude calibration

8.1. Background

The LBA buckling eigenmode has a long history of usage as an imperfection form in investigations of the nonlinear mechanics of imperfect structures that predate the widespread adoption of computational finite element analysis. As an imperfection it was relatively straightforward to define using basic mathematical functions and introduce into the governing differential equations that could then be solved directly [20,21], and for simpler systems such as columns or plates the bow-shaped buckling eigenmodes do indeed resemble gross geometric imperfections that could conceivably arise in construction. In the finite element era, an LBA requires only a relatively simple element formulation with limited treatment of geometric nonlinearity, is easy to perform as a singular value decomposition of a matrix system and almost always gives a physically meaningful result if membrane compression or shear is present in the pre-buckling stress state. Additionally, almost every finite element software now has a facility to import an eigenmode from one analysis to act as a scalable superimposed mesh imperfection in another. Consequently, such ‘eigenmode-affine’ imperfections have

acquired a status as a 'default' imperfection form to be used where none other can be conceived, a position also adopted by the previous EN 1993-1–6 [2] (although the upcoming prEN1993-1–6 [9] is more careful about cautioning the analyst that these may not be the most realistic or the most unfavourable to the structure), and often are the only imperfection that is explored.

Computed LBA eigenmodes are non-unique, sign-reversible, infinitely scalable and typically normalised by the software in some way before being reported to the user, for example to give a vector norm or peak nodal *dof* equal to unity (the convention will vary with the FE software). The calculation of a scaling factor, here called $SF_{GMNIA,imp}$, that is specific to a particular computed LBA eigenmode shape and that when imported as a scaled mesh perturbation into a GMNIA achieves an imperfection amplitude δ_0 compliant with prEN 1993-1–6 is not trivial and requires two prior calibrations to be performed. Here the subscript 'imp' is a qualifier indicating that the scaling is specific to the given imperfection model or the 'I' in 'GMNIA' (i.e. the specific eigenmode). The two calibrations are illustrated here on localised and global 'dimple' imperfections which are characterised by smooth shape deviations perpendicular to the mid-surface of the nominal perfect shell geometry and are often the most damaging for thin cylindrical shell structures dominated by axial compression. Here it is critical to distinguish between the *mathematical* amplitude δ_m which is a parameter of the imperfection model under the control of the analyst (referring here to the maximum amplitude of the eigenmode to be used for generation of the imperfection), and the *tolerance* amplitude δ_0 which is a measurement that can be done on the constructed structure using a specific gauge length to verify that a level of fabrication quality has been achieved in construction and is controlled by prEN1993-1–6 [9] or EN 1090–2:A1 [22]. This distinction was not well appreciated in the past and has been a frequent source of misinterpretations.

8.2. LBA eigenmode calibration

A first calibration considers the computed LBA eigenmode exactly as reported by the software, a 'default state' that is here always assumed to correspond to a scaling factor $SF = 1$. The calibration then relates the peak computed absolute modal displacement normal to the nominal midsurface of the perfect shell (δ_m) to unity as

$$c_{SF=1,imp} = \frac{1}{\delta_{m,SF=1,imp}} \tag{9}$$

which has dimensions of inverse length. This factor does not change if the eigenmode is sign-reversed, but it will be dependent on the normalisation performed by the software. It is frequently approximately unity.

A second calibration then relates the controllable δ_m to its corresponding achieved δ_0 as

$$c_{\delta,imp,s} = \frac{\delta_{m,imp,s}}{\delta_{0,imp,s}} \tag{10}$$

and must be established separately per sign direction s of the eigenmode. The values of $\delta_{m,imp,s}$ and $\delta_{0,imp,s}$ used in Eq. (10) may be established at any scaling factor without greatly affecting the resulting $c_{\delta,imp,s}$, although it is usually simplest to do in the default state at $SF = 1$. Finally, the scaling factor to be applied on the default LBA eigenmode so as to generate an equivalent geometric imperfection in a GMNIA is

$$SF_{GMNIA,imp,s} = s \cdot \delta_0 \cdot c_{SF=1,imp} \cdot c_{\delta,imp,s} \tag{11}$$

where δ_0 is the target amplitude of the dimple relative to the appropriate gauge length as defined by prEN 1993-1-6 and $s = \pm 1$ depending on whether the eigenmode is taken 'as computed' ($s = +1$) or 'sign-reversed' ($s = -1$). The prEN1993-1-6 [9] GMNIA provisions require the imperfection to be 'unfavourably oriented towards the centre of the shell curvature', and since an LBA eigenmode can be sign-reversed and still remain a valid mathematical solution corresponding to the same eigenvalue (R_{cr}), the possibility cannot be discounted that a sign-reversed LBA eigenmode may result in a more unfavourable imperfection. The calculation of $SF_{GMNIA,imp}$ is illustrated here on the critical LBA eigenmodes for both load cases as they are qualitatively very different. The variables introduced here are summarised in Table 5. It should also be noted that the scaling factor $SF_{GMNIA,imp}$ applied to the eigenmode shape to achieve a target tolerance amplitude δ_0 is *not* the same as the eigenvalue which is instead a scaling factor applied on the loads to achieve a singular stiffness matrix.

Table 5
Summary of LBA eigenmode calibration notation.

Entity	Description
$\delta_{m,SF=1,imp}$	Peak absolute modal displacement normal to the nominal perfect shell midsurface in the 'default state' (mode shape normalized as returned from FEA) at $SF = 1$ for the LBA eigenmode imperfection 'imp'
$c_{SF=1,imp}$	Calibration between actual $\delta_{m,SF=1,imp}$ and a target of unity for $SF = 1$
$\delta_{m,imp,s}$	Peak modal displacement at some SF for the LBA eigenmode imperfection 'imp' which is in a direction that is either 'as computed' ($s = +1$) or 'sign-reversed' ($s = -1$)
$\delta_{0,imp,s}$	Peak achieved (single-sided) tolerance amplitude under the same conditions as $\delta_{m,imp,s}$
$c_{\delta,imp,s}$	Calibration between controllable $\delta_{m,imp,s}$ and achieved $\delta_{0,imp,s}$ under the same conditions
δ_0	Target code-compliant GMNIA tolerance amplitude
$SF_{GMNIA,imp,s}$	Scaling factor on the eigenmode imperfection 'imp' to achieve a code-compliant GMNIA target δ_0 tolerance amplitude in direction s

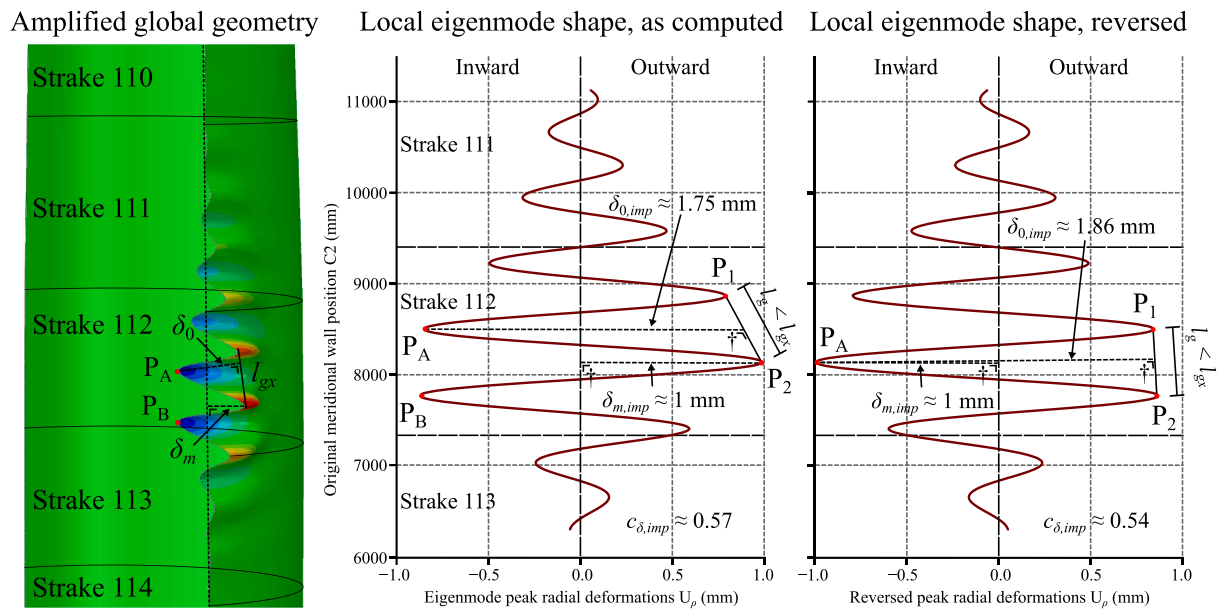

Fig. 5. Calculation of the calibration factors $c_{\delta,imp}$ for the first LBA eigenmode (localised) for LC1.
† this angle is a right angle even if it does not appear so on the figure due to differences in scale of the vertical and horizontal axes.

8.3. Calibration of a localised eigenmode (LC1)

For LC1, the critical LBA eigenmode is shown in detail in Fig. 5 where the peak eigenmode displacements are concentrated in Strake 112 where $r = 2750$ mm and $t = 15$ mm. At $SF = 1$ the peak radial displacement of this normalised eigenmode is reported by the ABAQUS software to be $U_{\rho,\max} \equiv \delta_{m,SF=1,\{LC1,LBA1\}} \approx 1$ mm, such that $c_{SF=1,\{LC1,LBA1\}} = 1 / \delta_{m,SF=1,\{LC1,LBA1\}} \approx 1\ \text{mm}^{-1}$. According to prEN1993-1–6 sub-clause 9.8.2, this eigenmode may be used as an equivalent geometric imperfection if it is scaled to result in a target tolerance amplitude of δ_0 relative to an appropriate gauge of length l_g which for eigenmodes dominated by meridional compression is given by

$$l_{gx} = 4\sqrt{rt} \tag{12}$$

and evaluates to ~ 812.4 mm for Strake 112. If a straight gauge is 'placed' against the imperfection (from the outside) at the worst possible location (passing through points P_1 and P_2 in Fig. 5 where $(U_{\rho,P1}, C_{2,P1}) \approx (0.80, 8874.24)$ and $(U_{\rho,P2}, C_{2,P2}) \approx (1.00, 8138.17)$ respectively when $SF = 1$, the Euclidean distance between which is $l_g \approx 736.1$ mm $< l_{gx}$), then the perpendicular distance between this straight gauge and the radially deepest point on the imperfect wall P_A where $(U_{\rho,PA}, C_{2,PA}) \approx (-0.85, 8488.68)$ can be calculated using classical geometry as

$$\delta_{0,\{LC1,LBA\},s} = \frac{\left|\left(U_{\rho,P2} - U_{\rho,P1}\right)\left(C_{2,P1} - C_{2,PA}\right) - \left(U_{\rho,P1} - U_{\rho,PA}\right)\left(C_{2,P2} - C_{2,P1}\right)\right|}{\sqrt{\left(U_{\rho,P2} - U_{\rho,P1}\right)^2 + \left(C_{2,P2} - C_{2,P1}\right)^2}} \tag{13}$$

which evaluates to ~ 1.75 mm when $SF = 1$. The calibration factor for this eigenmode if it is to be used as an imperfection is then $c_{\delta,\{LC1,LBA\},+1} = \delta_{m,\{LC1,LBA1\},+1} / \delta_{0,\{LC1,LBA1\},+1} \approx 1 / 1.75 \approx 0.57$ which indicates that the measured tolerance amplitude is almost twice that of the mathematical peak amplitude. It can be shown that another potential calculation involving point P_B where $(U_{\rho,PB}, C_{2,PB}) \approx (-0.87, 7752.61)$ would instead lead to a higher calibration factor of ~ 0.60 and an imperfection where the target δ_0 is exceeded at P_A leading to an overly conservative evaluated resistance. For a Fabrication Tolerance Quality Class (FTQC) of A or 'Excellent', the target tolerance amplitude is $\delta_0 = \delta_{0x} = 0.006 l_{gx} \approx 4.87$ mm leading to $SF_{GMNIA,\{LC1,LBA1\},+1} \approx 1 \times 4.87 \times 1 \times 0.57 \approx 2.79$. Illustrated on the right of Fig. 5, the same but sign-reversed eigenmode exhibits $\delta_{0,\{LC1,LBA1,rev\},-1} \approx 1.86$ mm for which $c_{\delta,\{LC1,LBA1\},-1} \approx 0.54 < c_{\delta,\{LC1,LBA1\},+1}$ and thus $SF_{GMNIA,\{LC1,LBA1\},-1} \approx -1 \times 4.87 \times 1 \times 0.54 \approx -2.63$. A summary of these calculations for FTQC A, B ('High') and C ('Normal') is presented in Table 6.

8.4. Calibration of a global eigenmode (LC2)

The provisions of prEN1993-1–6 recognise that eigenmode imperfections relating to torsional buckling modes do not generally occur in fabricated civil engineering shells, and permit such eigenmodes to be set aside as improbable or adopted at a laxer (though unspecified) target imperfection amplitude. These provisions notwithstanding, the calibration procedure for such eigenmodes is presented here for completeness due to its relative complexity. Illustrated in Fig. 6 for the torsional LBA eigenmode that is critical for

Table 6
Summary of dimple imperfection calibration factors for LBA eigenmodes.

LBA eigenmode imperfection	Gauge Type	Length [mm]	Calibration factors c_{SF} [mm^{-1}]	c_δ [-]	Target δ_0 [mm] FTQC A	FTQC B	FTQC C	Scaling factor SF_{GMNIA} [-] FTQC A	FTQC B	FTQC C
LC1,LBA1,+1	l_{gx}	812.4	1	0.57	4.87	8.12	13.0	2.79	4.65	7.44
LC1,LBA1,-1				0.54				−2.63	−4.38	−7.01
LC1,LBA1(simple)				0.50				±2.44	±4.06	±6.50
LC2,LBA1,+1	$l_{g\theta}$	2369.6	0.99	0.69	18.96	40.28	85.30	13.03	27.69	58.63
LC2,LBA1,-1				0.64				−12.05	−25.60	−54.22
LC2,LBA1(simple)			1	0.50				±9.48	±20.14	±42.65

LC2, the peak modal displacement occurs in Strake 106 at a vertical position of $C_2 = 23818.7$ mm and at a default scaling factor of $SF = 1$ has an outward radial value of $U_{\rho,\max} \equiv \delta_{m,SF=1,\{LC2,LBA1\}} \approx 1.01$ mm leading to $c_{SF=1,\{LC2,LBA\}} \approx 0.99\,\text{mm}^{-1}$. For eigenmodes dominated by circumferential compression or membrane shear, the relevant gauge is curved with radius of curvature equal to the local transverse radius $r \approx 2369.6$ mm at that vertical position and a curved gauge arc length

$$l_{g\theta} = \min\left\{2.3\sqrt[4]{H^2 rt}, r\right\} \tag{14}$$

which also evaluates to $r \approx 2369.6$ mm.

This gauge arc is 'placed' against the wall (from the outside) between points P_1 and P_2 which are identified by trial and error so as to identify the end points of an arc of approximately the required curved gauge arc length r. It may be noted from Fig. 6 that a gauge will not necessarily pass through the obvious outward maxima of the eigenmode. This arc spans a one-radian sector of a circle of radius r whose centre is located at O' and whose coordinates may be calculated through classical geometry as:

$$C_{1,O'} = \frac{1}{2}\left(C'_{1,P1} + C'_{1,P2}\right) - a\cdot\sin\alpha \quad \text{and} \quad C_{3,O'} = \frac{1}{2}\left(C'_{3,P1} + C'_{3,P2}\right) - a\cdot\cos\alpha \tag{15}$$

where

$$a = \sqrt{r^2 - b^2}, \quad b = \frac{1}{2}\sqrt{\left(C' - C'_{1,P2}\right)^2 + \left(C'_{3,P1} - C'_{3,P2}\right)^2}, \quad C'_{i,j} = C_{i,j} + U_{i,j} \quad \text{and} \quad \alpha = \tan^{-1}\left(\frac{C'_{3,P1} - C'_{3,P2}}{C'_{1,P2} - C'_{1,P1}}\right)$$

At $SF = 1$, O' is located at (C'$_{1,O'}$, C'$_{3,O'}$) ≈ (0.38, 0.36) while the points P_1 and P_2 are located approximately at (C'$_{1,P1}$, C'$_{3,P1}$) ≈ (404.83, 2335.15) and (C'$_{1,P2}$, C'$_{3,P2}$) ≈ (2176.53, 938.02). Subsequently, the perpendicular distance between this curved gauge and the radially deepest point on the imperfect wall P_A where (C'$_{1,PA}$, C'$_{3,PA}$) ≈ (1581.98, 1762.88) can be calculated using classical geometry as

$$\delta_{0,\{LC2,LBA\},s} = r - \sqrt{\left(C'_{1,O'} - C'_{1,PA}\right)^2 + \left(C'_{3,O'} - C'_{3,PA}\right)^2} \tag{16}$$

which evaluates to ~1.45 mm when $SF = 1$ and leads to a calibration factor c_δ for this eigenmode of $c_{\delta,\{LC2,LBA\}.+1} = \delta_{m,\{LC2,LBA1\}.+1} / \delta_{0,\{LC2,LBA1\},+1} \approx 1.01 / 1.45 \approx 0.70$.

For FTQC A, the target tolerance amplitude is thus $\delta_0 = \delta_{0\theta} = 0.008 l_{g\theta} \approx 18.96$ mm (conservatively assuming the higher dimple tolerance values from Table 9 in the prEN) such that the necessary scaling factor on this eigenmode is $SF_{GMNIA,\{LC2,LBA1\},+1} \approx 1 \times 18.96 \times 0.99 \times 0.70 \approx 13.03$. When the eigenmode is sign-reversed (Fig. 6, bottom) it may be similarly shown that $c_{\delta,\{LC2,LBA\},-1} = \delta_{m,\{LC2,LBA1\},-1} / \delta_{0,\{LC2,LBA1\},-1} \approx 1.01 / 1.57 \approx 0.64$ and therefore $SF_{GMNIA,\{LC2,LBA1\},-1} \approx -1 \times 18.96 \times 0.99 \times 0.64 \approx -12.05$. A summary of these calculations for critical LBA eigenmodes for both load cases and all three FTQC's is presented in Table 6. The computed GMNIA are explored in Section 10.

8.5. A simpler approach?

The above is admittedly an onerous procedure to be applied regularly for any load case and analysts may be tempted to simply assume $c_{SF} = 1$ (implicitly assuming that the eigenmode is scaled to a peak normal displacement of 'unity' by the solver) and $c_\delta = ½$ such that $SF_{GMNIA,imp,s} = ½s\delta_0$ for any LBA eigenmode imperfection. As illustrated in Table 6, this temptation should be resisted because it is not guaranteed to be conservative under all conditions. Here this assumption leads to scaling factors SF that are *lower* than those derived in the rigorous manner for either eigenmode and scaling direction and which would lead to GMNIA resistances that are unconservatively *higher* than they should be had the amplitude of the eigenmode imperfection been rigorously code-compliant. However, because of the nature of nonlinear behaviour it should *never* be assumed that a particular sign direction is more critical just because its $|SF_{GMNIA}|$ is higher (as illustrated shortly), and c_{SF} does not always evaluate approximately to unity. As a final caution given the complexity of the eigenmode geometries being considered, is it generally difficult to guarantee that a configuration leading to a higher $|SF_{GMNIA}|$ has not been missed somewhere. Consequently, it is recommended that analysts wishing to do this calibration frequently should write their own scripts or macros to automate this procedure which can execute a more rigorous exhaustive search

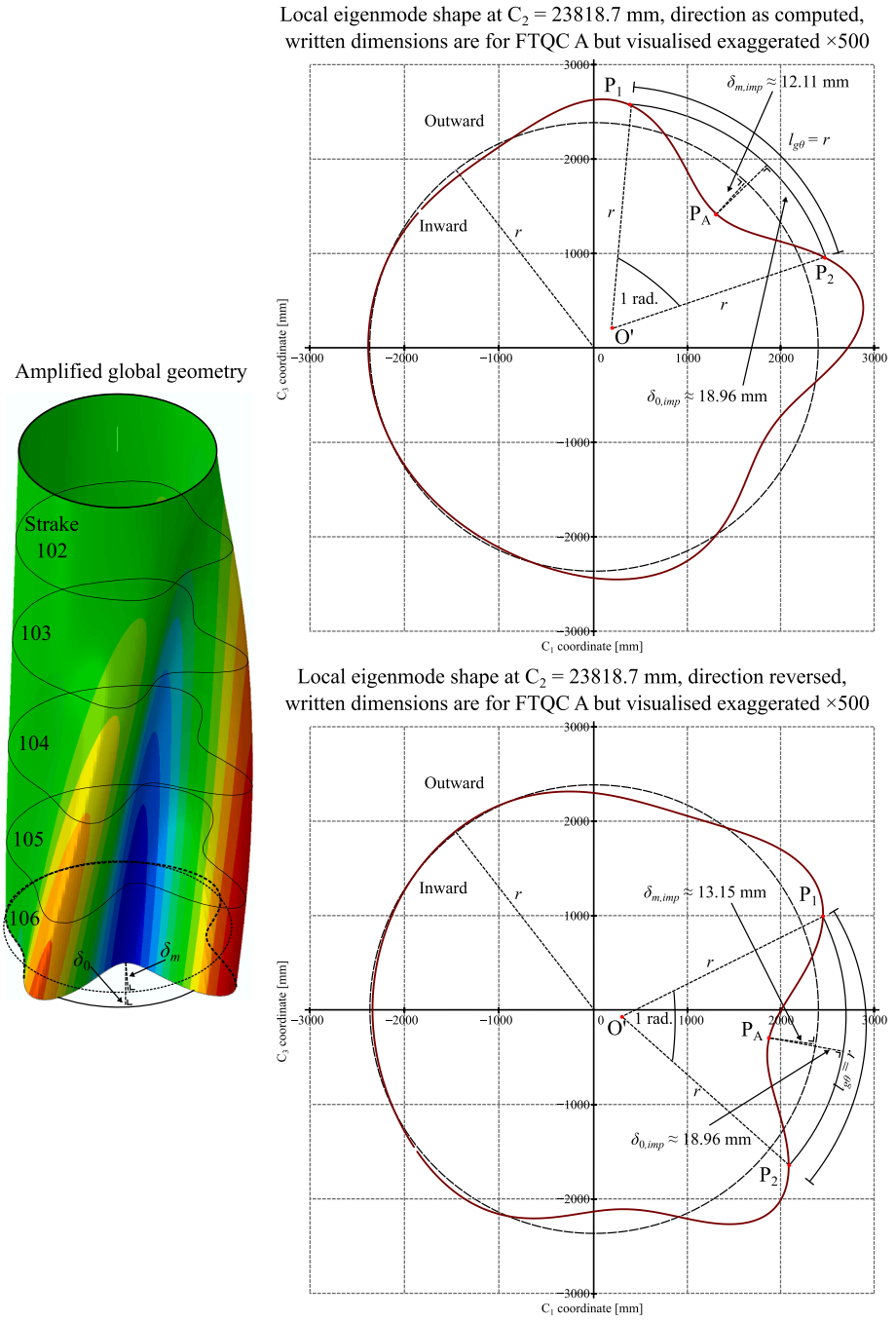

Fig. 6. Calculation of the calibration factor $c_{\delta,imp}$ for the first LBA eigenmode (global torsional) for LC2.

through the placement of 'virtual gauges' at all possible locations around the shell wall. The procedure is likely to be most straightforward for regular rectangular meshes constructed from quadrilateral shell elements where gauges automatically align with the element edges, and triangulations would require special handling.

9. GMNIA #2 with axisymmetric weld depression imperfections: Amplitude calibration

The Rotter and Teng [11] axisymmetric weld depression is an idealised model of the radially-inward curling of the edges of a cylindrical shell plate caused by anticlastic bending during rolling and additionally by shrinkage of a welded circumferential joint during cooling, suggested by field measurements to be a realistic representation of this manufacturing defect across a range of d/t ratios

[23–27]. Originally used to explore the mechanics of the stability of two-segment cylindrical shell with a single weld at the segment junction under uniform meridional compression and pressurisation, the weld depression model has since been widely used in more generalised form for multi-strake cylindrical silo structures where several weld instances are implemented at regular vertical locations [28–30]. The model has also been adapted in a naïve way for computational studies of multi-strake wind turbine support towers with both conical and cylindrical shell strakes [13,31], where the starting imperfect axisymmetric geometry of the entire tower was generated mathematically as

$$R(z) = r(z) - \sum_{j=1}^{k} \delta_{m,j} e^{-\frac{\pi}{\lambda_j}|z-z_j|} \left[\cos\left(\frac{\pi}{\lambda_j}|z-z_j|\right) + \sin\left(\frac{\pi}{\lambda_j}|z-z_j|\right) \right] \tag{17}$$

where

$$\lambda_j = \frac{\pi\sqrt{r(z_j)\,t_{j,\min}}}{\sqrt[4]{3(1-\nu^2)}}$$

such that $R(z)$ and $r(z)$ are the imperfect and nominally perfect radial geometries of the tower as a function of the vertical axis coordinate z respectively, k is the total number of individual weld depressions in the tower (currently 13, at the junctions of Strakes 102–103 to 114–115) every j-th one of which has a different vertical position z_j, associated bending half-wavelength λ_j (where $t_{j,\min}$ is the smallest of the two joining plate thicknesses) and mathematical imperfection amplitude $\delta_{m,j}$ such that $R(z_j) = r(z_j) - \delta_{m,j}$. A single weld depression extending $\sim 2\lambda_j$ on either side of the junction is illustrated in Fig. 7a where, in relation to the generic coordinate system presented in Fig. 1c, $z = C_2$ and $R = C_\rho = \sqrt{(C_1^2 + C_3^2)}$. This model is 'naïve' in the sense that the imperfection is always defined relative to the global radial direction rather than relative to the normal to the shell midsurface, making it simpler to program. When the shell is cylindrical the radial and normal directions are the same, but when it is conical, they are distinct. However, since conical strakes used in wind turbine support towers are usually very steep and 'near-cylindrical', any error in not rigorously correcting for the normal direction is likely negligible.

In contrast to the LBA eigenmode, the extent of the j-th individual weld depression imperfection is controlled directly via the model's mathematical amplitude $\delta_{m,j}$ and there is no need for a scaling factor SF. However, $\delta_{m,j}$ must still be calibrated to deliver a code-compliant target tolerance amplitude $\delta_{0,j}$ at the z_j location via a corresponding *local* factor $c_{\delta,j} = \delta_{m,j} / \delta_{0,j}$ relative to a local straight gauge of appropriate length $l_{g,j}$. This gauge is 'placed' against the outside of the wall between positions P_1 and P_2 whose coordinates can be expressed analytically using Eq. (17) as $(R(z_j + \Delta_j), z_j + \Delta_j)$ and $(R(z_j - \Delta_j), z_j - \Delta_j)$ respectively, where Δ_j is the gauge half-length projected on the vertical axis, such that $\delta_{0,j}$ is the perpendicular distance between point P_A at $(R(z_j), z_j)$ and this gauge:

$$\delta_{0,j} = \frac{\left|R(z_j - \Delta_j) + R(z_j + \Delta_j) - 2R(z_j)\right|\Delta_j}{\sqrt{\left(R(z_j - \Delta_j) - R(z_j + \Delta_j)\right)^2 + 4\Delta_j^2}} \tag{18}$$

The calibration involves the optimisation of both $c_{\delta,j}$ and Δ_j to minimise the absolute distance between $\delta_{0,j}$ calculated by Eq. (18) and the target δ_0 as required by prEN 1993-1-6, subject to the constraint that the Euclidian distance between P_1 and P_2 is equal to the

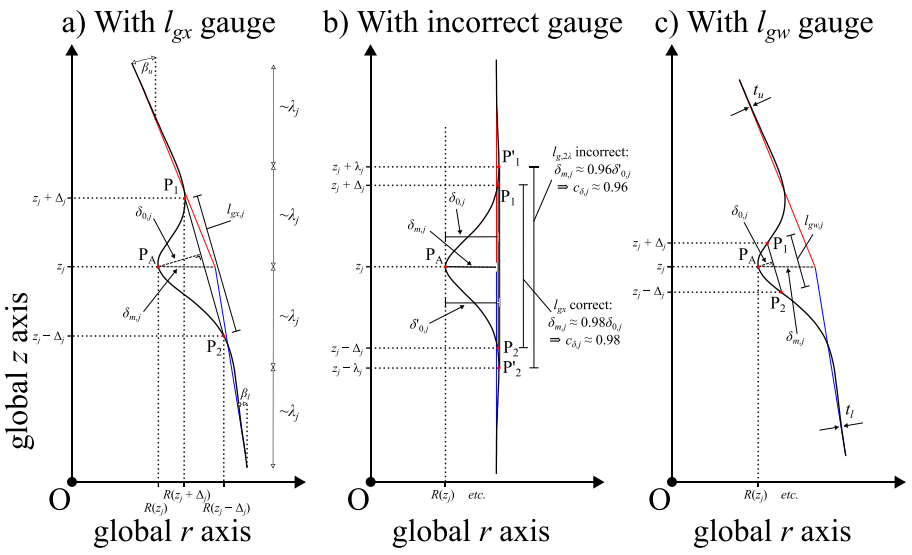

Fig. 7. Junction of two shell geometries with a naïve axisymmetric weld depression.

Table 7
Summary of naïve axisymmetric weld depression imperfections at each strake junction (13 in total) with target measurable tolerance amplitudes δ_0, calibration factors c_δ and mathematical peak amplitudes δ_m.

Weld at junction of Strakes, with l_{gx} and l_{gw}	FTQC	l_{gx} assuming $t = \min(t_u,t_l)$			l_{gw} assuming $t = \min(t_u,t_l)$		
		δ_0 [mm]	c_δ [-]	δ_m [mm]	δ_0 [mm]	c_δ [-]	δ_m [mm]
102 & 103	A	3.99	0.90	3.57	1.95	1.43	2.79
$l_{gx} = 665.45$ mm	B	6.66	0.93	6.18	3.25	1.48	4.82
$l_{gw} = 325$ mm	C	10.65	0.95	10.08	5.20	1.51	7.86
103 & 104	A	4.06	0.98	3.98	1.95	1.59	3.09
$l_{gx} = 675.95$ mm	B	6.76	0.98	6.63	3.25	1.59	5.16
$l_{gw} = 325$ mm	C	10.82	0.98	10.62	5.20	1.59	8.25
104 & 105	A	4.28	0.98	4.19	2.10	1.55	3.26
$l_{gx} = 712.69$ mm	B	7.13	0.98	6.97	3.50	1.55	5.44
$l_{gw} = 350$ mm	C	11.40	0.98	11.16	5.60	1.55	8.70
105 & 106	A	4.34	0.98	4.24	2.10	1.58	3.31
$l_{gx} = 723.69$ mm	B	7.24	0.98	7.07	3.50	1.58	5.52
$l_{gw} = 350$ mm	C	11.58	0.98	11.32	5.60	1.58	8.84
106 & 107	A	4.40	0.98	4.30	2.10	1.60	3.36
$l_{gx} = 733.49$ mm	B	7.33	0.98	7.17	3.50	1.60	5.60
$l_{gw} = 350$ mm	C	11.75	0.98	11.48	5.60	1.60	8.97
107 & 108	A	4.46	0.98	4.36	2.10	1.63	3.41
$l_{gx} = 744.12$ mm	B	7.44	0.98	7.27	3.50	1.63	5.69
$l_{gw} = 350$ mm	C	11.91	0.98	11.64	5.60	1.63	9.11
108 & 109	A	4.69	0.98	4.59	2.25	1.59	3.58
$l_{gx} = 781.05$ mm	B	7.81	0.98	7.64	3.75	1.59	5.97
$l_{gw} = 375$ mm	C	12.50	0.98	12.23	6.00	1.59	9.55
109 & 110	A	4.75	0.98	4.64	2.25	1.61	3.63
$l_{gx} = 791.67$ mm	B	7.92	0.98	7.74	3.75	1.61	6.05
$l_{gw} = 375$ mm	C	12.67	0.98	12.38	6.00	1.61	9.68
110 & 111	A	4.81	0.98	4.71	2.25	1.64	3.68
$l_{gx} = 802.12$ mm	B	8.02	0.98	7.84	3.75	1.64	6.14
$l_{gw} = 375$ mm	C	12.83	0.98	12.55	6.00	1.64	9.82
111 & 112†	**A**	**4.87**	**2.05**	**10.00**	**2.25**	**3.48**	**7.84**
$l_{gx} = 812.40$ mm	**B**	**8.12**	**1.62**	**13.18**	**3.75**	**2.75**	**10.33**
$l_{gw} = 375$ mm	**C**	**13.00**	**1.38**	**17.94**	**6.00**	**2.34**	**14.06**
112 & 113	A	4.87	0.98	4.76	2.25	1.66	3.73
$l_{gx} = 812.40$ mm	B	8.12	0.98	7.94	3.75	1.66	6.22
$l_{gw} = 375$ mm	C	13.00	0.98	12.71	6.00	1.66	9.96
113 & 114	A	5.03	0.98	4.92	2.40	1.60	3.84
$l_{gx} = 839.05$ mm	B	8.39	0.98	8.20	4.00	1.60	6.41
$l_{gw} = 400$ mm	C	13.42	0.98	13.12	6.40	1.60	10.25
114 & 115	A	5.03	0.98	4.92	2.40	1.60	3.84
$l_{gx} = 839.05$ mm	B	8.39	0.98	8.20	4.00	1.60	6.41
$l_{gw} = 400$ mm	C	13.42	0.98	13.12	6.40	1.60	10.25

† See discussion in Section 10.

appropriate gauge length l_g. A separate calibration must be performed per weld and per FTQC, though it is straightforward to implement in Excel using the SOLVER functionality. A summary of each such result is presented in Table 7, where the calibration is done once for the gauge length given by l_{gx} in Eq. (12) appropriate for shells dominated by meridional compression and, for completeness, again for a much shorter meridional gauge length l_{gw} given by:

$$l_{gw} = 25t \tag{19}$$

This shorter gauge is prescribed in prEN1993-1–6 for the assessment of tolerances in constructed shells with circumferential welds of r/t ratio<400. Although it is not strictly required for GMNIA calculations, making it so was once an item of discussion and for this reason its effect is explored here. In both cases the thickness is chosen as that of the thinnest strake at the junction, $t = \min(t_u,t_l)$ where t_u and t_l are the thicknesses of the upper and lower strakes respectively, leading to a slightly shorter gauge length and a slightly more lenient amplitude.

Some important observations can be made on the basis of Table 7. At every junction between two strakes where the change in angle of incline is negligible ($d\beta = |\beta_1 - \beta_2| = O(10^{-3})$ for each junction except Strakes 102–103 and 111–112, see Table 1 for β values), the calibration factor c_δ relative to the longer l_{gx} gauge is approximately unity, meaning that $\delta_m \approx \delta_0$ is both a convenient and conservative approximation that was de facto assumed in previous studies [32,33]. In certain previous parametric studies of weld depressions in cylindrical shells involving the first Author [34,35] it was slightly incorrectly assumed (though with different notation) that $c_\delta \approx 1/1.04 \approx 0.96$ based on an effective gauge length of $l_{g,2\lambda} \approx 2\lambda \approx 4.9\sqrt{(rt)}$, the distance between the two outermost crests of the weld depression on either side of the midline (Fig. 7b), which is ~ 22 % longer than the code-compliant $l_{gx} = 4\sqrt{(rt)}$ (Eq. (12)). This led to adopted mathematical amplitudes δ_m calibrated relative to $l_{g,2\lambda}$ that were ~ 2 % smaller than they would have been had the calibration been performed relative to the code-compliant l_{gx}.

Table 8
Summary of GMNIA #1 & #2 with mathematical scaling factors *SF* to achieve target imperfection amplitudes δ_0&δ_m) critical load proportionality factors.

Analysis	Imperfection	FTQC & etc.	LC1 LPF		LC2 LPF	
LBA ($\equiv R_{cr}$)	*n/a*	*n/a*	2.901		1.401	
MNA ($\equiv R_{pl}$)			1.807		1.868	
GMNA			1.167		1.256	
GMNIA #1 (with LBA eigenmode imperfections sourced from either load case; "LBA1" indicates that the first reported eigenmode has been used)	LC1,LBA1,+1 (non-reversed)	A, $SF \approx 2.79$	1.061*		1.131*	
		B, $SF \approx 4.65$	0.928		0.989	
		C, $SF \approx 7.44$	0.823		0.880	
	LC1,LBA1,-1 (sign-reversed)	A, $SF \approx -2.63$	1.056		1.123	
		B, $SF \approx -4.38$	0.916		0.979	
		C, $SF \approx -7.01$	0.812		0.867	
	LC2,LBA1,+1 (non-reversed)	A, $SF \approx 13.03$	*n/a*		1.067*	
		B, $SF \approx 27.69$	*n/a*		0.895	
		C, $SF \approx 58.63$	*n/a*		0.666	
	LC2,LBA1,-1 (sign-reversed)	A, $SF \approx -12.05$	*n/a*		1.032	
		B, $SF \approx -25.60$	*n/a*		0.868	
		C, $SF \approx -54.22$	*n/a*		0.649	
GMNIA #2 (with naïve weld depression imperfections)	Welds relative to gauge l_{gx}	A	1.040*	1.140†	1.121	1.174†
		B	0.930	1.011†	1.002	1.037†
		C	0.803	0.857†	0.862*	0.873†
	Welds relative to gauge l_{gw}	A	1.127	1.186†	1.214	1.220†
		B	1.030	1.080†	1.110	1.110†
		C	0.906	0.941†	0.964	0.962†

* The corresponding incremental buckling modes are shown in Fig. 8.
† For a model with a simplified treatment of the strake 111–112 junction.

Where $d\beta$ is not negligible then simply assuming $c_\delta \approx 1$ may be very incorrect, such as at the junction of Strakes 102 &103 ($d\beta \approx 0.12°$) where it would be mildly conservative but particularly at the junction of Strakes 111 & 112 ($d\beta \approx 1.51°$, the 'sharpest' change in incline where the tower transitions from a cylindrical to a conical strake) where it would be very unconservative. For the much shorter l_{gw} gauge, it is remarkable that the depression must be made to be quite 'deep' to achieve the target δ_0 (Fig. 7c) with all c_δ significantly exceeding unity, although the required δ_m are consistently smaller than those necessary for the longer l_{gx} gauge. The relationship between c_δ and the FTQC is nonlinear, and it is thus recommended that no value of c_δ should be assumed *a priori* for conical geometries and that the calibration be performed rigorously each time using the minimisation procedure outlined above. However, in contrast to LBA eigenmodes, the calibrations are fully independent of the loads and need only be done once per structure. It is once again recommended to implement this procedure in an automated script or macro for convenience and consistency.

10. GMNIA #1 & #2: Comparison of computed resistances

10.1. GMNIA #1 with LBA eigenmode imperfections

The computed GMNIA resistances of the tower under both cases and with different LBA eigenmode imperfections are summarised in Table 8, performed under identical solver settings as the GMNAs. Firstly, the non-reversed critical LBA eigenmode for LC1 (Fig. 5) was used as an imperfection in GMNIAs performed under both load cases for each of the three FTQCs. The 'dimple-like' nature of this eigenmode supports its use as a plausible equivalent imperfection for either load case and may be thought of as a model of a random local defect at a potentially unfavourable location. The imperfect tower design resists the loading but only at the highest FTQC A with GMNIA resistances falling below unity for FTQC B and C. Importantly, though the sign-reversed eigenmode requires a *smaller* $|SF_{GMNIA}|$ to achieve a target δ_0 compliant with a particular FTQC than when non-reversed, for each FTQC it actually leads to slightly *lower* computed GMNIA resistances. This counter-intuitive result suggests that it is generally not possible to determine which eigenmode sign direction will be the most unfavourable on the basis of the magnitude of the scaling factor alone, and both possibilities must be explored.

Equilibrium relationships for GMNIA with the reversed eigenmodefrom LC1 at FTQC A are presented as blue curves and squares in Fig. 3 and are representative of all computed results. Similar to GMNA, they illustrate a very linear initial response followed by an elastic–plastic bifurcation buckling event that the ABAQUS solver was generally unable to follow into the post-buckling domain due to reported convergence issues. A selection of incremental buckling modes (given by the difference between the global deformation state just after and just before the buckling event characterised by a reduction in the LPF) are illustrated in the first three examples in Fig. 8 (corresponding to those resistances marked with an asterisk '*' in Table 8). These are typical of all such computed results and illustrate that the GMNIA will most likely buckle into a mode similar in shape and location to the LBA eigenmode which was introduced as an imperfection. Lastly, although the critical torsional LBA eigenmode from LC2 is generally thought to be too improbable to be a realistic imperfection form, at code-compliant scaling factors it is quite a damaging one and leads to lower GMNIA resistances for LC2 than the dimple-like critical eigenmode from LC1. It, too, here is worse still when sign-reversed, leading to GMNIAs below unity for all FTQC B and C.

Table 9
Additional robustness GMNIA calculations (all FTQC A).

Analysis	Imperfection	Conditions	LC1 LPF	LC2 LPF
LBA ($\equiv R_{cr}$)	*n/a*	*n/a*	2.901	1.401
MNA ($\equiv R_{pl}$)			1.807	1.868
GMNA			1.167	1.256
GMNIA #1	LC1,LBA1,+1	$SF \approx 2.79$	1.061*	1.131*
	(non-reversed)	90 % of amplitude	1.088	1.160
		Follower loads	1.082	1.154
	LC1,LBA1,-1	$SF \approx -2.63$	1.056	1.123
	(sign-reversed)	90 % of amplitude	1.084	1.157
		Follower loads	1.077	1.150
	LC1,LBA9,+1	$SF \approx 2.94$	1.103	*n/a*
	LC1,LBA9,-1	$SF \approx -2.61$	1.117	*n/a*
	LC1,LBA13,+1	$SF \approx 2.36$	1.048	*n/a*
	LC1,LBA13,-1	$SF \approx -2.34$	1.048	*n/a*
	LC1,LBA94,+1	$SF \approx 2.27$	1.166	*n/a*
	LC1,LBA94,-1	$SF \approx -2.13$	1.166	*n/a*
	LC2,LBA1,+1	$SF \approx 13.03$	*n/a*	1.067*
	(non-reversed)	90 % of amplitude	*n/a*	1.086
		Follower loads	*n/a*	1.073
	LC2,LBA1,-1	$SF \approx -12.05$	*n/a*	1.032
	(sign-reversed)	90 % of amplitude	*n/a*	1.049
		Follower loads	*n/a*	1.039
GMNIA #2	Welds relative to gauge l_{gx}	Table 6 amplitudes	1.040*	1.121
		90 % of amplitude	1.079	1.161
		Follower loads	1.060	1.144

* The corresponding incremental buckling modes are shown in Fig. 8.

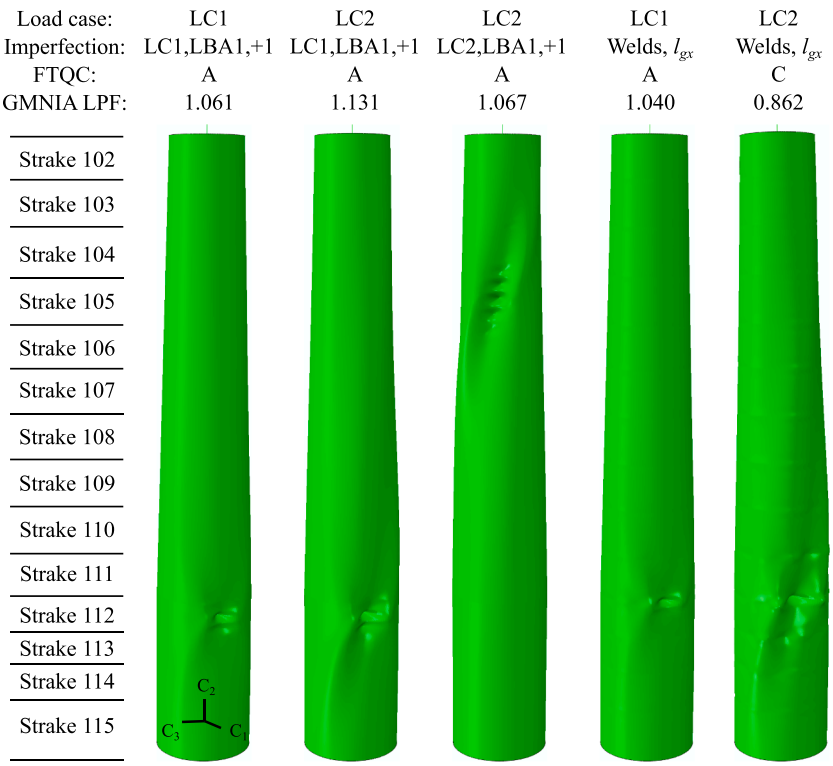

Fig. 8. GMNIA incremental buckling modes for both load cases and imperfections.

10.2. GMNIA #2 with axisymmetric weld depression imperfections

The computed GMNIA resistances for the models with multiple axisymmetric weld depression imperfections are summarised in Table 8, again performed under identical solver settings as the GMNAs. A representative pair of incremental buckling modes is given in the last two examples of Fig. 8, which consistently identify the region of Strakes 111–112 as critical under both load cases. When the imperfections are defined relative to the l_{gx} gauge, the resulting GMNIA resistances are quite comparable with those obtained for the critical LC1 LBA eigenmode although for FTQC A and C they are more conservative. Relative to the shorter l_{gw} gauge, the resistances are all expectedly higher, a finding that suggests that this shorter gauge length need *not* be prescribed for use in GMNIA analyses even for thicker shells with $r/t < 400$. The analyses were found to suffer from the same convergence difficulties beyond the first buckling event, as reflected in the orange curves and squares in Fig. 3.

The interested reader may wish to consider the single weld imperfection at the junction between Strakes 111 & 112 more closely. The non-negligible discontinuity in the meridional incline $d\beta$ angle at this location potentially poses a problem of interpretation for a straight gauge l_g of any length, since as mathematical amplitude $\delta_m \to 0$ the geometry of the weld as defined by Eq. (17) becomes such that a meaningful tolerance amplitude δ_0 eventually stops being well-defined. Although the c_δ calibration illustrated in Table 7 is mathematically correct, it could potentially be argued that it is not physically meaningful and that an 'angular gauge' that followed the nominal meridional incline may instead be a more appropriate reference device at this location. Were such a device to have been used, the calibration would once again have been closer to $c_\delta \approx 1$ such that $\delta_m \approx \delta_0$. Given that this location is also structurally the most critical, a second set of GMNIA was performed for both load cases assuming $\delta_m = \delta_0$ at this location. Presented in Table 8 but marked with a '†', the resulting resistances are from between 4 and 10 % and 0 to 5 % higher for LC1 and 2 respectively (with one result surprisingly being slightly lower) showing that some gains in resistance can be made with this possibly more physically realistic treatment. However, this speculative illustration should be taken with caution, since an angular gauge would have likely required a different code-compliant δ_0 to have been defined with it and this issue will be looked into during future EN 1993-1-6 development.

10.3. Additional robustness calculations

As a sanity check, the analyst should use the buckling reduction curves in prEN 1993-1-6 to *estimate* the dimensionless buckling knockdown factor $\chi = R_k/R_{pl}$ to have a rough reference point against which the GMNIA calculations may be compared via the ratio R_{GMNIA}/R_{MNA}. The dimensionless slenderness $\lambda = \sqrt{(R_{pl}/R_{cr})}$ may be estimated as $\sqrt{(R_{MNA}/R_{LBA})}$ to give ~ 0.79 and ~ 1.16 for LC1 and LC2 respectively. For LC1, when this estimate is introduced into either the axial compression or bending capacity curves in Annexes D and E of the prEN respectively, and if reasonable assumptions are made regarding the average r and t together with a conservative dimensionless length of $\Omega \approx 1.09$ (see Table 1 in the companion paper [37]) then it may be estimated that $\chi \approx 0.62$ and 0.57 for the two capacity curves respectively for FTQC A. This is entirely commensurate with the typical R_{GMNIA}/R_{MNA} ratios seen in Table 8. For LC2, if the capacity curve for shear is used then it may similarly be estimated that $\chi \approx 0.56$ which is again consistent with the GMNIA predictions. This ballpark agreement serves to give some confidence in the integrity of the calculations.

An additional array of GMNIA calculations were performed to the purposes of code compliance and to permit a final structural assessment of the tower segment to be made. These calculations were limited to FTQC A only assuming both the eigenmode and weld depression imperfections (l_{gx} gauge only, Table 7 amplitudes). Firstly, prEN 1993-1-6 requires the analyst to verify that an imperfection amplitude 10 % smaller than the target δ_0 does not unexpectedly lead to lower GMNIA LPF. This phenomenon is known to happen for shells under complex unsymmetrical load cases (see Fig. 13 in [29] Sadowski and Rotter (2011a) or numerous figures in [36] Sadowski and Rotter (2013)) which exhibit very nonlinear pre-buckling responses. However, as the pre-buckling path is here very linear in all cases (Fig. 3), this phenomenon it is not expected to be present and indeed GMNIA computed at 90 % of the code-compliant imperfection amplitudes are in all cases less conservative (Table 9). Secondly, the analyst is required to confirm that 'follower' load effects (i.e. loads which 'follow' the rotational *dof* at the nodes at which they are applied) are either improbable or insignificant. The design loads for both LCs originate either due to wind or to gravity, neither of which should physically lead to 'follower' effects. Additionally, when such effects are incorporated into the tip point loads, the resulting GMNIA load factors are in fact slightly unconservative.

An important final robustness check concerns the validity of the choice of LBA eigenmode imperfection, in particular of the 'localised' kind as computed for LC1. To mitigate against the risk of missing the possibility that a (modestly) higher-order LBA eigenmode could act as a more severe GMNIA imperfection, prEN 1993-1-6 suggests that a 'sufficient number' of LBA eigenmodes should be extracted and examined. An estimate can be made of the imperfection sensitivity of any shell strake in the segment by calculating $\alpha \cdot R_{cr}$ for it and identifying an overall minimum, and to ensure that an eigenmode that has deformations in this location is trialled in a GMNIA. Here R_{cr} is the elastic critical buckling resistance for that strake while $\alpha = \alpha_G \cdot \alpha_I$ is the product of an elastic reduction factor due to geometric nonlinearity α_G and one due to imperfection sensitivity α_I. Algebraic expressions may be found for these parameters in Annexes D and E for the reference system of a uniform cylinder under uniform axial compression and uniform bending respectively. It may be verified using the geometry in Table 1 that regardless of the equations used, α is approximately constant for each strake and these are therefore approximately similarly imperfection sensitive. The product $\alpha \cdot R_{cr}$ does gradually decrease as r and t decrease with height to attain a minimum for Strake 102, but this is only a consequence of R_{cr} being calculated for a much simpler cylindrical reference system than the complex tower segment and should for this benchmark *not* be interpreted as a sign that an LBA eigenmode with buckling deformations localised near the tower top will be a particularly bad imperfection. The algebraic approach should be treated here only as indicative.

A more thorough exploration was performed as follows. The first 100 LBA eigenmodes were extracted for LC1 and examined (Fig. 9). It was found that 57 % of eigenmodes have buckling deformations localised in the vicinity of Strakes 111 and 112 which have

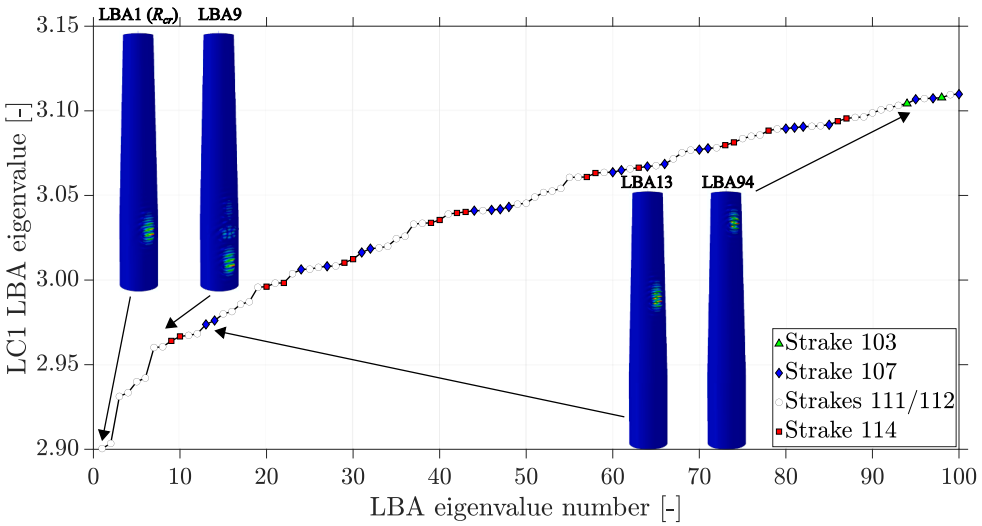

Fig. 9. An analysis of the first 100 LBA eigenmodes for LC1.

been consistently found to be most critical in GMNIA (Figs. 2 & 7). The next most critical regions are Strake 114 (18 % of eigenmodes, first appearing as the 9th eigenmode with an eigenvalue of 3.028, see Table 4) and Strake 107 (23 % of eigenmodes, first appearing as the 13th eigenmode with an eigenvalue of 3.048). Only 2 % of eigenmodes occur near the top of the tower where $\alpha \cdot R_{cr}$ is roughly at a minimum (first appearing as the 94th eigenmode with an eigenvalue of 3.309). If the 9th, 13th and 94th eigenmodes are used as imperfections in GMNIA at the appropriately calibrated amplitudes for FTQC A (termed LBA9, LBA13 and LBA94 respectively, see Table 9), the surprising result emerges that the 13th eigenmode is a *slightly* more critical imperfection than the first for LC1. It is generally not possible to detect such an eventuality except by direct investigation as shown here, and it may be quite onerous to extract the necessary number of eigenmodes without specialist modelling schemes such as the 'hybrid' beam-shell methodology detailed in Sadowski [13]. The analysis above was not repeated for LC2 since torsional eigenmodes are usually discounted as unrealistic, but a similar outcome is possible in principle. This example serves to illustrate that LBA eigenmode imperfections are in fact non-trivial to work with if a globally critical form is sought, and there is still no evidence that *any* of the eigenmode geometries considered here correspond to physically realistic systematic or random imperfections that actually occur during full-scale construction.

10.4. Design resistance assessment

After the robust set of GMNIA performed above, it is now possible to make an informed decision as to whether the present tower segment design is acceptable at the buckling ultimate limit state for FTQC A. Assuming for the purposes of this illustration that $k_{\mathrm{GMNIA}} = 1$ (it is stressed that this value is at least in part dependent on the analyst's skill in reproducing a known result, see discussion in the Introduction) such that $R_k = R_{\mathrm{GMNIA}}$ (Eq. (2)), then the tower segment passes the check if $R_d \geq 1$ or if $R_k \geq \gamma_{\mathrm{M}} = 1.1$ (assuming the Eurocode 3 partial factor for stability). It may be concluded that the segment is generally *not* acceptable under LC1 except for the case of the most lenient interpretation of the weld depression imperfection amplitudes at the critical junction between Strakes 111 and 112. It *is* acceptable under LC2 except if the unrealistic LC2 LBA torsional eigenmode is used as an imperfection. It is stressed that the present design was chosen for illustration purposes only and does not correspond to a structure that has actually been constructed.

11. Conclusions and recommendations

This paper has presented a detailed worked reference solution to the benchmark problem recently used in an international 'round-robin' computational shell buckling exercise. The publication of this reference solution is intended to initialise a public repository of accumulated realistic benchmark problems for the verification and calibration of finite element models of full-scale civil engineering metal shells. This is particularly pertinent in light of new prEN 1993-1-6 and prEN 1993-1-14 both of which include rules for the standardisation of the use of finite element analysis in structural steel design and consequently place a significant emphasis on model verification and calibration.

The provisions of prEN 1993-1-6 for GMNIA calculations are particularly challenging and require the careful calibration of imperfection models so as to achieve a code-compliant imperfection amplitude. A particular distinction should be made between a 'mathematical' imperfection amplitude under the control of the analyst, and a 'tolerance' imperfection amplitude which is what could be measured in the completed structure. Establishing a calibration between the two is non-trivial, and the calibration procedure is illustrated here on three qualitatively different imperfection forms. These include a localised computed linear bifurcation buckling eigenmode, a global computed eigenmode with torsional deformations and an axisymmetric weld depression imperfection generated using algebraic formulae. These require the careful processing of imperfection models using provided formulae derived using classical

geometry.

A number of specific recommendations for code-compliant GMNIAs are as follows:

- A meshing protocol conditioned on the Koiter ellipse gives an automated way to create meshes that scale appropriately with the tower geometry [13].
- LBA eigenmodes are an obvious but somewhat risk-prone imperfection candidate for GMNIAs. Multiple higher-order eigenmodes corresponding to buckling deformations at different parts of the structure should be trialled to mitigate the very real possibility that the 'critical' (i.e. first) computed eigenmode may *not* be a globally critical imperfection in a GMNIA. This is particularly the case for eigenmodes which are localised in nature. Torsional eigenmodes can generally be discounted as unrealistic, as can any eigenmode geometries that clearly do not correspond to any physically realistic systematic or random imperfections.
- Idealised weld depression imperfections may be readily adopted as design imperfections for GMNIAs as they are realistic models of systematic construction-relevant imperfections and are appropriately conservative for near-cylindrical shells that are predominantly governed by meridional compression. This is also consistent with the algebraic buckling curves in prEN 1993-1-6 [9] for meridional compression and bending buckling, both of which have been derived assuming weld depression imperfections. For the purposes of comparison, it is advised to use these in tandem with GMNIAs where at least a handful of LBA eigenmodes were used as imperfections. If significant deviations are found, it should be considered which sets of results should be used in design.
- The correct implementation of weld imperfections with code-compliant amplitudes at conical transitions, particularly where there is a non-negligible change in the meridional incline angle, remains a matter of discussion. The use of a straight measurement gauge at such locations to establish the reference amplitude may not be entirely appropriate if this leads to unreasonably large deviations from the nominal geometry. Smaller amplitudes may be considered if reasonably argued and if accompanied by special quality control measures during construction.

Declaration of Competing Interest

The authors declare that they have no known competing financial interests or personal relationships that could have appeared to influence the work reported in this paper.

Data availability

The authors are unable or have chosen not to specify which data has been used.

Acknowledgements

The Authors warmly acknowledge the intellectual legacies of Prof. J. Michael Rotter and Prof. Herbert Schmidt, both former Convenors of CEN/TC250/WG6, and Prof. Richard Greiner who were major contributors to the ground-breaking EN 1993-1-6 Standard on the Strength and Stability of Metal Shells. The work presented here builds on their many ideas, concepts and advances. Shoulders of giants, and all that.

The Authors are additionally grateful to Matthias Baeßler, Ingmar van Dijk, Claas Fischer, Frithjof Marten, Lijithan Kathirkamanathan and Tim Rutkowski for their comments on the draft manuscript.

References

[1] ECCS EDR5#2 (2013) "Buckling of steel shells – European Design Recommendations" 5th Edition, 2nd Impression, Eds J.M. Rotter & H. Schmidt, *European Convention for Constructional Steelwork*, ECCS, Brussels.
[2] EN 1993-1-6 (2007) "Eurocode 3: Design of Steel Structures, Part 1-6: Strength and Stability of Steel Structures" *Commité Européen de Normalisation*, CEN, Brussels.
[3] ENV 1993-1-6 (1999) "Eurocode 3: Design of steel structures, Part 1-6: General rules – Supplementary rules for the strength and stability of shell structures" *Comité Européen de Normalisation*, CEN, Brussels.
[4] A.J. Sadowski, M.T. Morata, L. Kathirkamanathan, M. Seidel, J.M. Rotter, On the existing test dataset of isotropic cylindrical metal shells and the design of modern metal civil engineering shells, Struct. Saf. 102 (2022), 102285, https://doi.org/10.1016/j.strsafe.2022.102285.
[5] Arbocz J. & Abramovich H. (1979) "The initial imperfection data bank at the Delft University of Technology. Part I." *Technical Report No. LR-290*, Delft University of Technology.
[6] Dancy R. & Jacobs D. (1988) "The initial imperfection data bank at the Delft University of Technology. Part II." *Technical Report No. LR-559*, Delft University of Technology.
[7] Kathirkamanathan L., Sadowski A.J., Seidel M. & Schafer B.W. (2022) "Recommendations for surface imperfection surveys for thin-walled metal wind turbine support towers" *Proc. Int. Offshore Wind Technical Conf. ASME*, IOWTC2022, Dec 7-8, Boston, Massachusetts.
[8] prEN 1993-1-14 (2021) "Eurocode 3: Design of steel structures, Part 1-14: Design assisted by finite element analysis" Document N3437 Approved for CEN Enquiry, *Comité Européen de Normalisation*, CEN, Brussels.
[9] prEN 1993-1-6 (2021) "Eurocode 3: Design of steel structures, Part 1-6: Strength and stability of steel structures" Document N3518 Approved for CEN Enquiry, *Comité Européen de Normalisation*, CEN, Brussels.
[10] Teng J.G. & Rotter J.M. (2004) "Buckling of Thin Metal Shell" (Compendium of Chapters), *Spon Press*.
[11] J.M. Rotter, J.G. Teng, Elastic stability of cylindrical shells with weld depressions, ASCE J. Struct. Eng. 115 (5) (1989) 1244–1263.
[12] A.J. Sadowski, L. Potoschnig, P. Constantinou, The 'panel analysis' technique in the computational study of axisymmetric thin-walled shell systems, Finite Elem. Anal. Des. 152 (2018) 55–68.
[13] A.J. Sadowski, On the advantages of hybrid beam-shell structural finite element models for the efficient analysis of metal wind turbine support towers, Finite Elem. Anal. Des. 162 (2019) 19–33.

[14] A. Spagnoli, Koiter circles in the buckling of axially compressed conical shells, Int. J. Solids Struct. 40 (2003) 6095–6109.
[15] ABAQUS (2017) "ABAQUS 2017 Commercial Finite Element Software and Documentation" *Dassault Systèmes*, Simulia Corporation, Providence, RI, USA.
[16] Rotter J.M. (2004) "Buckling of cylindrical metal shells under axial compression" Chapter 2 In J.G. Teng, J.M. Rotter (Eds), Buckling of thin metal shells, *Spon Press*.
[17] C. Doerich, J.M. Rotter, Accurate determination of plastic collapse loads from finite element analyses, J. Press. Vessel. Technol. 133 (1) (2011) 011202.
[18] A.J. Sadowski, O.K. Fajuyitan, J. Wang, A computational strategy to establish algebraic parameters for Reference Resistance Design of metal shell structures, Adv. Eng. Softw. 109 (2017) 15–30.
[19] G.B. dos Santos, L. Gardner, M. Kucukler, A method for the numerical derivation of plastic collapse loads, Thin-Walled Struct. 124 (2018) 258–277.
[20] W.T. Koiter, The stability of elastic equilibrium, PhD Thesis, Technical University of Delft (1945).
[21] W.T. Koiter, The effect of axisymmetric imperfections on the buckling of cylindrical shells under axial compression, Proc. Koninklijke Nederl. Akademie Wetenschappen 66 (5) (1963) 265–279.
[22] EN 1090-2:A1 (2018) "Execution of Steel Structures and Aluminium Structures – Technical Requirements for Steel Structures" *Commité Européen de Normalisation*, CEN, Brussels.
[23] Rotter J.M. (1996) "Elastic plastic buckling and collapse in internally pressurised axially compressed silo cylinders with measured axisymmetric imperfections: interactions between imperfections, residual stresses and collapse", *Proc. International Workshop on Imperfections in Metal Silos: Measurement, Characterisation and Strength Analysis*, CA-Silo, Lyon, 119-140.
[24] J.M. Rotter, Shell structures: the new European standard and current research needs, Thin-Walled Struct. 31 (1998) 3–23.
[25] P.A. Berry, J.M. Rotter, R.Q. Bridge, Compression tests on cylinders wit axisymmetric weld depressions, ASCE J. Eng. Mech. 126 (4) (2000) 405–413.
[26] M. Pircher, P.A. Berry, X. Ding, R.Q. Bridge, The shape of circumferential weld-induced imperfections in thin-walled steel silos and tanks, Thin-Walled Struct. 39 (2001) 999–1014.
[27] J.G. Teng, X. Lin, J.M. Rotter, X.L. Ding, Analysis of geometric imperfections in full-scale welded steel silos, Eng. Struct. 27 (2005) 938–950.
[28] A.J. Sadowski, J.M. Rotter, Study of buckling in steel silos under eccentric discharge flows of stored solids, ASCE J. Eng. Mech. 136 (6) (2010) 769–776.
[29] A.J. Sadowski, J.M. Rotter, Buckling of very slender metal silos under eccentric discharge, Eng. Struct. 33 (2011) 1187–1194.
[30] A.J. Sadowski, J.M. Rotter, Steel silos with different aspect ratios: I – behaviour under concentric discharge, J. Constr. Steel Res. 67 (2011) 1537–1544.
[31] A.J. Sadowski, A. Camara, C. Málaga-Chuquitaype, K. Dai, Seismic analysis of a tall metal wind turbine support tower with realistic geometric imperfections, Earthq. Eng. Struct. Dyn. 46 (2017) 201–219.
[32] J. Wang, O.K. Fajuyitan, M.A. Orabi, J.M. Rotter, A.J. Sadowski, Cylindrical shells under uniform bending in the framework of Reference Resistance Design, J. Constr. Steel Res. 166 (2020) 105920.
[33] A.M. Mehretehran, S. Maleki, Axial buckling of imperfect cylindrical steel silos with isotropic walls under stored solids loads: FE analyses versus Eurocode provisions, Eng. Fail. Anal. 137 (2022) 106282.
[34] O.K. Fajuyitan, A.J. Sadowski, Imperfection sensitivity in cylindrical shells under uniform bending, Adv. Struct. Eng. 21 (16) (2018) 2433–2453.
[35] O.K. Fajuyitan, A.J. Sadowski, M.A. Wadee, J.M. Rotter, Nonlinear behaviour of short elastic cylindrical shells under global bending, Thin-Walled Struct. 124 (2018) 574–587.
[36] A.J. Sadowski, J.M. Rotter, Exploration of novel geometric imperfection forms in buckling failures of thin-walled metal silos under eccentric discharge, Int. J. Solids Struct. 50 (2013) 781–794.
[37] A.J. Sadowski, M. Seidel, H. Al-Lawait, E. Azizi, H. Balscheit, M. Böhm, L. Chen, I. van Dijk, C. Doerich-Stavridis, O.K. Fajuyitan, A. Filippidis, A.W. Fischer, C. Fischer, S. Gerasimidis, H. Karampour, L. Kathirkamanathan, F. Marten, Y. Mihara, S. Mishra, V. Sakharov, A. Shahini, S. Subramanian, C. Topkaya, H.N. R. Wagner, J. Wang, J. Wang, K.K. Yadav, X. Yun, P. Zhang, 8-MW wind turbine tower computational shell buckling benchmark. Part 1: An international 'round-robin' exercise, Eng. Fail. Anal. 148C (2023) 107124, https://doi.org/10.1016/j.engfailanal.2023.107124.